Qeios

Aerodynamic Design and Performance Analysis of Mars Ascent Vehicles

[1]Eretia Mwaene https://orcid.org/0009-0008-2472-6750

[2]Lazarus Obed Livingstone Banda* https://orcid.org/0000-0002-3436-6137

[1]Beijing Institute of Technology, School of aerospace engineering, Zhongguancun Campus, Beijing, China

[2]Beijing Institute of Technology, Graduate School of Education, Liangxiang Campus, Beijing, China

Corresponding author: lazaruslivingstonebanda@gmail.com

Abstract

The mid-lift-to-drag ratio vehicle possesses larger dimensions and enhanced aerodynamic characteristics compared to the conventional sphere-cone reentry vehicle, suggesting its suitability for crewed missions to Mars. This research employs Computational Fluid Dynamics (CFD) simulations to investigate the influence of varying geometries on the aerodynamic properties of mid-lift-to-drag ratio vehicles. The aerodynamic analysis of four distinct configurations demonstrates that a bow shock wave forms on the windward side, leading to a reduction in flow velocity and subsequent increases in pressure and temperature after the shock wave. The simulation results for the four configurations in both laminar and turbulent flow conditions, specifically using the Shear-Stress Transport (SST) model, reveal that turbulence results in higher aerodynamic heating compared to laminar flow. Moreover, the aerodynamic heating is greater at a 40° angle of attack than at 30°. In this study, the transition phenomena of four geometric

https://doi.org/10.32388/VJ9NX

configurations are examined using the k-ω-γ transition model. The findings indicate a pronounced transition to turbulence on the windward side of the Ellipsled 2.00-0.25 and Hammerhead-Nominal configurations under conditions of high Reynolds numbers, transitioning from laminar to turbulent flow. The investigation into the aerodynamic characteristics of mid-lift-to-drag ratio vehicles holds substantial importance for ensuring the safety and success of Martian reentry missions, highlighting the critical nature of aerodynamic behavior in the context of space exploration.
Keywords: Mid lift-to-drag ratio vehicle; Heat flux; Transition, Computational Fluid Dynamics

Introduction

Aerodynamics, the study of gas behavior in response to moving objects, primarily delves into the effects of drag and lift as air moves over and around solid structures. Given that air is the most prevalent gas encountered, it becomes a focal point in aerodynamic considerations. Engineers utilize principles of aerodynamics in designing an array of objects, from bridges and buildings to sports equipment. However, the aerodynamics of vehicles, such as airplanes and cars, assumes critical importance. Aerothermodynamics, studying the interplay between air motion and heat transfer during high-velocity flights, is vital in the design of flight vehicles.

Aerothermodynamics, especially relevant in hypersonic flight, scrutinizes the severe conditions air molecules endure, leading to significant compression and heating due to intense friction and shock waves. This results in considerable thermal loads on the vehicle, making the study of hypersonic aerothermodynamics crucial for improving thermal protection and performance of these vehicles. This field's strategic importance is highlighted in its application to military vehicles and missiles, enabling rapid, long-range strike capabilities (Jortner & Priya, 2018).

Hypersonic vehicles are engineered to withstand the rigors of extreme speeds and

temperatures, presenting substantial technological challenges in their design and construction. The dynamics of gas compression and resultant heating at hypersonic speeds necessitate advanced thermal management strategies. The thermal protection system (TPS) in such vehicles is critical, designed to shield against intense heat and protect from space debris. As the pursuit of reusable launch vehicles and space exploration intensifies, the development of an efficient and cost-effective TPS becomes increasingly paramount (Uyanna & Najafi, 2020).

SpaceX's Starship, intended for missions to the Moon, Mars, and beyond, exemplifies cutting-edge application of aerodynamics and material science in spacecraft design. Its aerodynamic configuration is crucial for its performance across various conditions, including the capability for vertical takeoff and landing. The choice of materials, like the advanced stainless steel alloy, reflects the emphasis on durability and reusability, essential for the sustainability of long-term space missions (Forder Bradley, 2022).

In summary, the exploration of aerodynamics and aerothermodynamics is fundamental in engineering disciplines, particularly in designing vehicles for Earth's atmosphere and space. The ongoing advancements in these fields are pivotal for the future of aerospace technology, enabling the expansion of human activity into space and enhancing the capabilities of hypersonic and space travel.

Review, 31(4), 27-39.

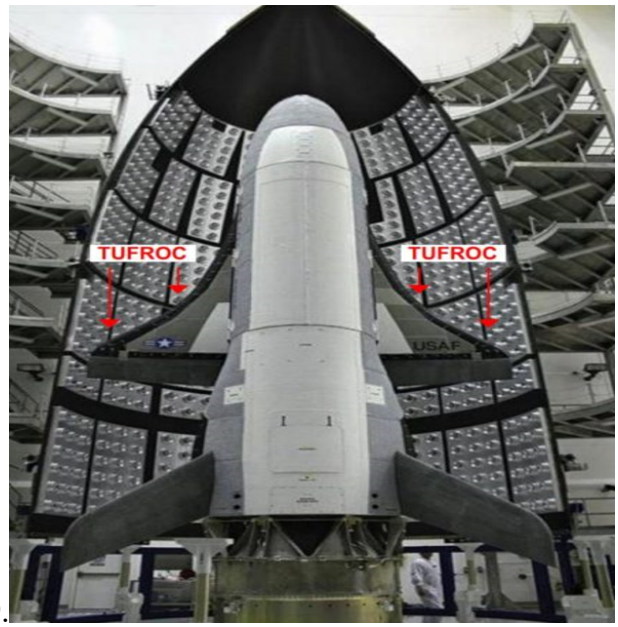

Figure 1 TUFROC design for thermal resistance. Originally developed for NASA. Eventually used by the AirForceX-37B as the wing leading edge

The thermal protection system, known as TUFROC (Toughened Uni-piece Fibrous Reinforced Oxidation-Resistant Composite), engineered at NASA Ames, is designed to withstand extreme temperatures up to 1,650 degrees Celsius, with a capability to endure peak temperatures of approximately 1,700°C (3,100°F). This material has garnered interest for its potential application in SpaceX's BFR (Starship/Super Heavy) project, particularly for the Starship's heat shield. TUFROC, characterized by its robustness in reusable entry conditions withstanding over 1,600°C (2,900°F) and possessing a single-use threshold of at least 2,000°C (3,600°F), was initially developed for NASA's X-37 program and subsequently employed in the Air Force X-37B for its wing leading edge (WLE). This composite demonstrates a temperature tolerance comparable to carbon/carbon composites but is significantly more cost-effective and quicker to produce.

Addressing the formidable challenges of space exploration, which range from conceptual to nascent stages of development, necessitates innovative solutions. The realization of these solutions,

crucial for advancing space exploration, will demand a spectrum of innovations from engineering and integration methodologies in spacecraft design to advanced architectural capabilities, constrained only by our imagination. A paradigm shift, facilitating these advancements, will enable the achievement of ambitious space exploration goals. Enhanced entry, descent, and landing (EDL) efficiency is identified as a critical priority, with improvements in EDL facilitating the delivery of larger payloads, improved surface accessibility, and precise landing capabilities that support the deployment of multiple assets at a single site.

Furthermore, reducing the costs of space travel will require the development of more efficient methods and reusable launch systems. Current spacecraft and launch vehicles lack the integration of technologies essential for extensive missions and the achievement of cost reductions in launch operations. To address this, NASA and its partners must transition from conceptualization to practical application, gaining insights through the design, development, manufacturing, implementation, and flight testing of robotic and crewed space vehicles, thus providing safer and more reliable capabilities (Fu et al., 2018).

It is advocated that an approach encompassing the integrated development and deployment of three revolutionary capabilities within an advanced entry vehicle framework, with potential applications in launch vehicle stage recovery, should be pursued. These innovations involve the integration of ultrasonic aero-propulsive maneuvering, the use of advanced asymmetrical launch shrouds, and the development of novel adaptable thermal insulation materials on ML-DREVs. These technological shifts are closely aligned with ongoing research in launch vehicle stage return, pursued by the Air Force and various commercial space entities. The realization of these integrated paradigms is essential for developing an entry vehicle system that fully leverages the synergies of multiple technologies, enabling NASA to conduct exploratory missions to planetary atmospheres

(Keys et al., 2006).

Figure 2 Vehicle reentry

The reentry process for such vehicles, as depicted in Figure 2, involves Mid-Lift-to-Drag Ratio Vehicles (ML-DREVs) that are typically designed with a streamlined shape to minimize air resistance, thereby reducing the drag coefficient. This design enhancement not only increases the vehicle's speed and efficiency but also lowers fuel consumption. ML-DREVs, with their distinctive and aesthetically pleasing designs, resonate with people's futuristic and science fiction-inspired sensibilities, attributing to them a certain cultural and historical significance. The larger dimensions of ML-DREVs enable the accommodation of increased cargo, making them suitable for extensive missions to Mars. These vehicles exhibit a higher lift-to-drag ratio and superior aerodynamic properties compared to traditional reentry capsules (Wang et al., 2007). During reentry, these characteristics allow for more effective deceleration and landing, significantly enhancing flight safety. Consequently, the aerodynamic performance of ML-DREVs holds considerable importance for the success and safety of crewed space exploration missions.

Reference:

- Wang, L., et al. (2007). Aerodynamic characteristics and design considerations for mid-lift-to-drag ratio reentry vehicles. Journal of Spacecraft and Rockets, 44(2), 400-410.

Research Objectives

In this study, we investigate the aerodynamic properties of mid-lift-to-drag ratio entry vehicles with varying configurations, focusing on the assessment of aerodynamic forces, thermal loads, and transition predictions. The research utilizes two distinct geometries: Ellipsled and Hammerhead (Hollis & Hollingsworth, 2013). The Ellipsled Geometry is explored through three configurations: Ellipsled-2.00-1.00, Ellipsled-2.00-0.50, and Ellipsled-2.00-0.25, each depicted in Figures 3, 4, and 5, respectively. Conversely, the Hammerhead Geometry is represented by a single configuration, termed the Hammerhead-Nominal Configuration, illustrated in Figure 6. The

subsequent sections provide an in-depth analysis of these configurations.

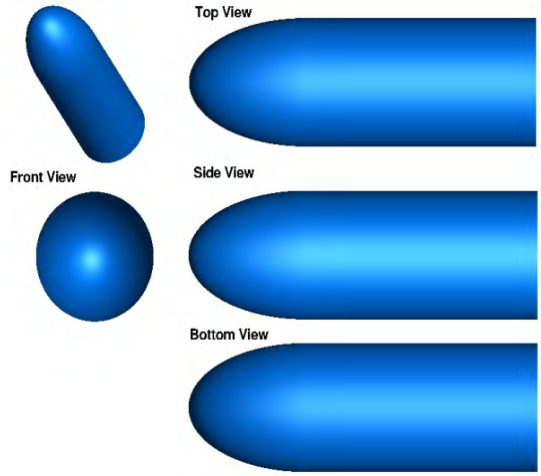

Figure 3 Schematic of Ellipsled-2.00-1.00 Configuration

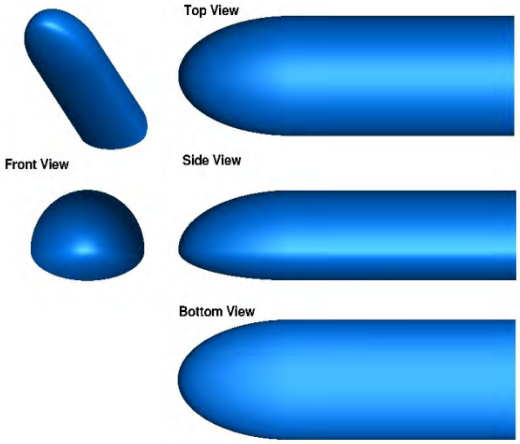

Figure 4 Schematic of Ellipsled-2.00-0.50 Configuration

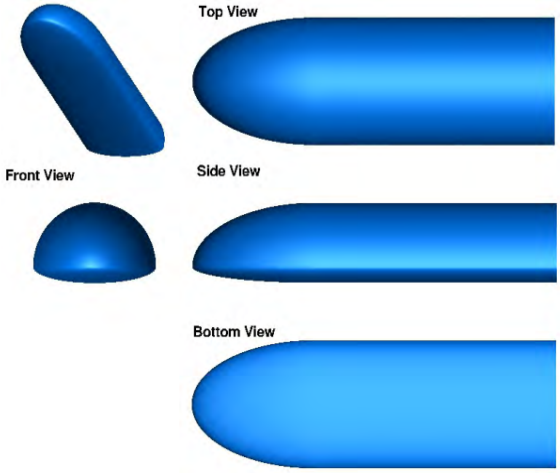

Figure 5 Schematic of Ellipsled-2.00-0.25 Configuration

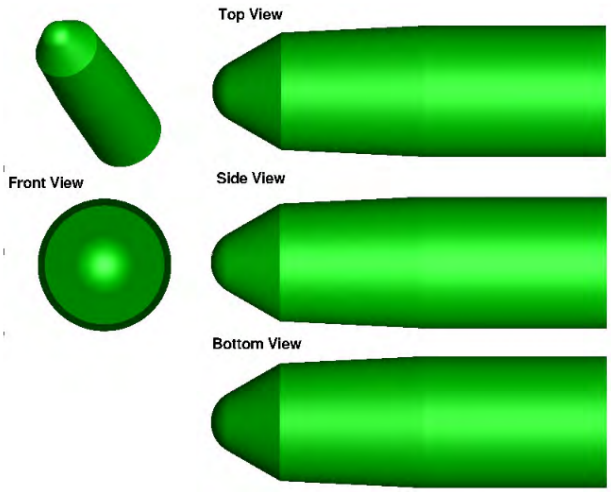

Figure 6 Schematic of Hammerhead-Nominal Configuration

The geometric parameters are defined in Figure 7 and Figure 8 and listed in Table 1 and Table 2.

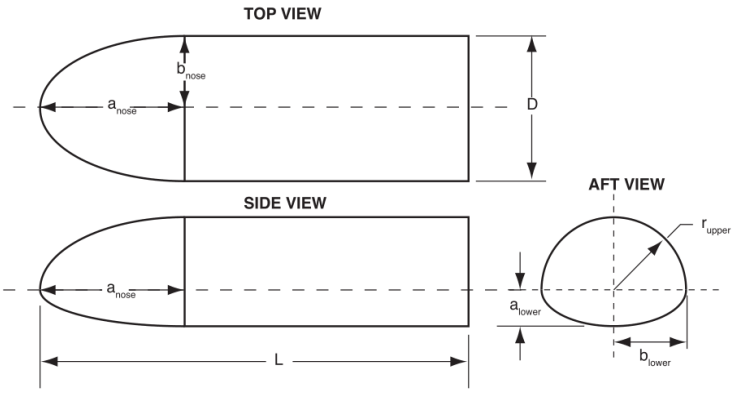

Figure 7 Ellipsled Geometry Definition

Table 1 Ellipsled geometry parameters

Geometry	L, in	D, in	a_{nose}, in	b_{nose}, in	a_{lower}, in	b_{lower}, in	r_{upper}, in
2.00-1.00	12.00	4.00	4.00	2.00	2.00	2.00	2.00
2.00-0.50	12.00	4.00	4.00	2.00	1.00	2.00	2.00
2.00-0.25	12.00	4.00	4.00	2.00	0.50	2.00	2.00

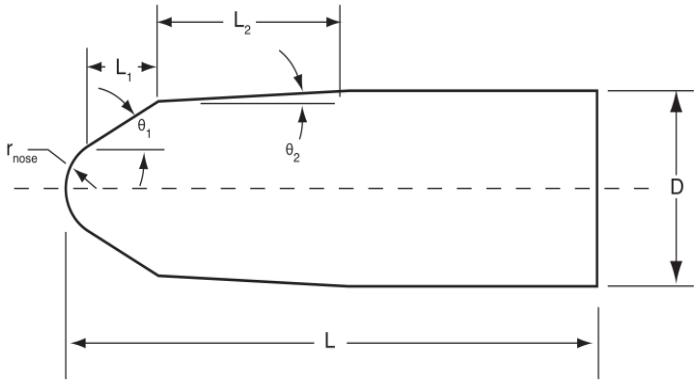

Figure 8 Hammerhead Geometry Definition

Table 2 Hammerhead geometry parameters

Geometry	L, in	D, in	r_{nose}, in	θ_1,deg	θ_2,deg	L_1,in	L_2,in
Hammerhead-blunt	12.00	4.00	1.25	30.00	0.8781	1.4750	4.2981

The calculation conditions at Mach 6 wind tunnel test are shown in **Error! Reference source not found.**.

Table 3 Nominal conditions for NASA Langley 20 In. Mach 6 Air Tunnel Test

α, deg	$Re_\infty, 1/m$	M_∞	P_∞, Pa	T_∞, K	ρ_∞, kg/m^3	U_∞,m/s	$h_{FR}, kg/m^2/s$
40	9.87×10^6	5.97	687	54.8	4.380×10^{-2}	882.2	2.336×10^{-1}
40	1.57×10^7	5.99	1129	56.1	7.034×10^{-2}	895.0	3.013×10^{-1}
40	2.24×10^7	6.02	1667	57.4	1.016×10^{-2}	908.0	3.685×10^{-1}
40	2.49×10^7	6.02	1879	58.1	1.132×10^{-2}	913.8	3.921×10^{-1}
40	2.73×10^7	6.03	2091	58.6	1.249×10^{-2}	918.2	4.172×10^{-1}

This research delves into the aerodynamic forces, thermal effects, and transition phenomena of four distinct configurations, utilizing Computational Fluid Dynamics (CFD) simulations to discern the most aerodynamically efficient shapes for Mars exploration missions. CFD, a sophisticated analytical tool, enables the quantitative prediction of fluid flow events through digital computation, grounded in the fundamental principles of fluid mechanics.

1) Aerodynamic Force: Aerodynamic force plays a pivotal role in the flight dynamics of a vehicle, significantly affecting its performance and stability (Wu, 1981). In this study, the lift-to-drag ratios of the four configurations are computed to identify those with superior aerodynamic properties. The variations in aerodynamic forces are examined under different flow conditions and angles of attack, underlining their criticality in the flight of mid-lift-to-drag ratio entry vehicles.

2) Aerodynamic Heat: At hypersonic speeds, the vehicle's surface encounters both laminar and turbulent flows, each affecting the aerodynamic heating differently (Daryabeigi, 2002). Through CFD analysis, the research assesses the aerodynamic heating on the surfaces of different configurations under various conditions, comparing the thermal impacts of laminar and turbulent flows on these vehicles.

3) Transition: The transition phenomenon, particularly at critical angles of attack, leads to a loss of lift and stability, manifesting as extensive postural instability and severe twisting movements, posing a significant risk to flight safety (Office U. Aviation and the Environment, 2001). This transition can be classified into flat-tailed and non-flat-tailed types. The former occurs when the aft flat area is insufficient, compromising tail wing control and stability. The latter, non-flat-tailed transition, involves adequate aft flat area but still results in lift loss and stall due to compressed airflow at the wing's leading edge under critical attack angles.

The study's focus on the transition effects under various operational conditions aims to enhance understanding of these phenomena, guiding the design and manufacturing of aircraft to mitigate transition-related safety risks.

METHODOLOGY

In the study, we used Tecplot, computational fluid dynamics (CFD),

We use the h_{FR} as the heat transfer coefficient obtained based on the Fay-Riddell theory, which we use to measure the degree of convective heat transfer. We represent the boundary layer fluid so that, when h_{FR} changes dramatically, we are able to judge the occurrence of transition, thus determining its location. Using Tecplot software for post-processing, we analyze the flowfield distribution, and aerodynamic heating curves, including the transition of the four shapes at 30° and 40° Angles of attack, respectively, and extract the midline data for comparison. We carry out the simulations using the CFD software system.

Governing equation

The general curvilinear coordinate system is usually used when the flow problem is studied (Tu Jiyuan et al., 2019). In general, curvilinear coordinates, the differential form of three-

dimensional unsteady compressible N-S equations after dimensionless is as follows:

$$\frac{\partial \hat{\boldsymbol{Q}}}{\partial t}+\frac{\partial\left(\hat{\boldsymbol{F}}-\hat{\boldsymbol{F}}_{v}\right)}{\partial \xi}+\frac{\partial\left(\hat{\boldsymbol{G}}-\hat{\boldsymbol{G}}_{v}\right)}{\partial \eta}+\frac{\partial\left(\hat{\boldsymbol{H}}-\hat{\boldsymbol{H}}_{v}\right)}{\partial \zeta}=0 \tag{3-1}$$

In the equation, the conservative variable vector is:

$$\hat{\boldsymbol{Q}}=\frac{\boldsymbol{Q}}{J}=\frac{1}{J}\begin{pmatrix}\rho\\ \rho u\\ \rho v\\ \rho w\\ \rho e\end{pmatrix} \tag{3-2}$$

Where the determinant of the Jacobian matrix transformed from the Cartesian coordinate system$(x, y, z)$to a general curvilinear coordinate system$\left(\xi, \eta, \zeta\right)$is：

$$J=\left|\frac{\partial(\xi, \eta, \zeta, t)}{\partial(x, y, z, t)}\right|=\left|\frac{\partial(x, y, z, t)}{\partial(\xi, \eta, \zeta, t)}\right|^{-1} \tag{3-3}$$

Define the inverter speed:

$$\begin{cases}U_{c}=\xi_{x} u+\xi_{y} v+\xi_{z} w+\xi_{t}\\ V_{c}=\eta_{x} u+\eta_{y} v+\eta_{z} w+\eta_{t}\\ W_{c}=\zeta_{x} u+\zeta_{y} v+\zeta_{z} w+\zeta_{t}\end{cases} \tag{3-4}$$

The invisco-vector flux is:

$$\hat{\boldsymbol{F}}=\frac{\boldsymbol{F}}{J}=\frac{1}{J}\begin{pmatrix}\rho U_{c}\\ \rho U u+\xi_{x} p\\ \rho U v+\xi_{y} p\\ \rho U w+\xi_{z} p\\ (\rho e+p) U-\xi_{t} p\end{pmatrix}, \hat{\boldsymbol{G}}=\frac{\boldsymbol{G}}{J}=\frac{1}{J}\begin{pmatrix}\rho V_{c}\\ \rho V u+\eta_{x} p\\ \rho V v+\eta_{y} p\\ \rho V w+\eta_{z} p\\ (\rho e+p) V-\eta_{t} p\end{pmatrix}, \hat{\boldsymbol{H}}=\frac{\boldsymbol{H}}{J}=\frac{1}{J}\begin{pmatrix}\rho W_{c}\\ \rho W u+\zeta_{x} p\\ \rho W v+\zeta_{y} p\\ \rho W w+\zeta_{z} p\\ (\rho e+p) W-\zeta_{t} p\end{pmatrix} \tag{3-5}$$

For an ideal gas:

$$p=\left(\gamma_g-1\right)\left[\rho e-\frac{\rho}{2}u_i u_i\right] \tag{3-6}$$

γ_g is specific heat ratio, 1.4 for air. The viscous vector flux is:

$$\hat{\boldsymbol{F}}_v=\frac{\boldsymbol{F}_v}{J}=\frac{1}{J}\begin{pmatrix}0\\ \xi_x\tau_{xx}+\xi_y\tau_{xy}+\xi_z\tau_{xz}\\ \xi_x\tau_{xy}+\xi_y\tau_{yy}+\xi_z\tau_{yz}\\ \xi_x\tau_{xz}+\xi_y\tau_{yz}+\xi_z\tau_{zz}\\ \xi_x b_x+\xi_y b_y+\xi_z b_z\end{pmatrix}$$

$$\hat{\boldsymbol{G}}_v=\frac{\boldsymbol{G}_v}{J}=\frac{1}{J}\begin{pmatrix}0\\ \eta_x\tau_{xx}+\eta_y\tau_{xy}+\eta_z\tau_{xz}\\ \eta_x\tau_{xy}+\eta_y\tau_{yy}+\eta_z\tau_{yz}\\ \eta_x\tau_{xz}+\eta_y\tau_{yz}+\eta_z\tau_{zz}\\ \eta_x b_x+\eta_y b_y+\eta_z b_z\end{pmatrix}$$

$$\hat{\boldsymbol{H}}_v=\frac{\boldsymbol{H}_v}{J}=\frac{1}{J}\begin{pmatrix}0\\ \zeta_x\tau_{xx}+\zeta_y\tau_{xy}+\zeta_z\tau_{xz}\\ \zeta_x\tau_{xy}+\zeta_y\tau_{yy}+\zeta_z\tau_{yz}\\ \zeta_x\tau_{xz}+\zeta_y\tau_{yz}+\zeta_z\tau_{zz}\\ \zeta_x b_x+\zeta_y b_y+\zeta_z b_z\end{pmatrix} \tag{3-7}$$

Based on the hypothesis of eddy viscosity, shear stress is the aggregate of viscous stress and Reynolds stress; the viscous stress and heat flux can be expressed as:

$$\tau_{ij}^{L}=\left(\frac{Ma_\infty}{\mathrm{Re}_\infty}\right)\mu\left[\left(u_{i,j}+u_{j,i}\right)-\frac{2}{3}u_{k,k}\delta_{ij}\right] \tag{3-8}$$

μ is the molecular viscosity coefficient, obtained from the Sutherland formula, $\mu=T^{1.5}\left(1+C_s\right)/\left(T_0+C_s\right)$, where $T_0=288.15K$, $C_s=110.4/T_\infty$ and T_∞ is the dimensional incoming flow temperature.

Reynolds shear stress of the linear vortex-viscous model is:

$$\tau_{ij}^{T}=\left(\frac{Ma_{\infty}}{\mathrm{Re}_{\infty}}\right)\left[\mu_{t}\left(u_{i,j}+u_{j,i}-\frac{2}{3}u_{k,k}\delta_{ij}\right)-\frac{2}{3}\rho k\delta_{ij}\right] \tag{3-9}$$

$k=0.5u_{i}u_{i}$ is the total pulsating kinetic energy μ_{t} and s the viscosity coefficient of the turbulent vortex.

All the above physical quantities are dimensionless, and the characteristic variables are the characteristic length $\tilde{L}$ and free parameters of incoming flow, including density $\tilde{\rho}_{\infty}$, sound velocity $\tilde{a}_{\infty}$, temperature $\tilde{T}_{\infty}$, and viscosity coefficient $\tilde{\mu}_{\infty}$. The dimensionless forms of each physical quantity are as follows

$$x=\frac{\tilde{x}}{\tilde{L}},y=\frac{\tilde{y}}{\tilde{L}},z=\frac{\tilde{z}}{\tilde{L}},u=\frac{\tilde{u}}{\tilde{a}_{\infty}},v=\frac{\tilde{v}}{\tilde{a}_{\infty}},w=\frac{\tilde{w}}{\tilde{a}_{\infty}}$$
$$\rho=\frac{\tilde{\rho}}{\tilde{\rho}_{\infty}},e=\frac{\tilde{e}}{\tilde{a}_{\infty}^{2}},p=\frac{\tilde{p}}{\tilde{\rho}_{\infty}\tilde{a}_{\infty}^{2}},T=\frac{\tilde{T}}{\tilde{T}_{\infty}},\mu=\frac{\tilde{\mu}}{\tilde{\mu}_{\infty}},t=\frac{\tilde{t}}{\tilde{L}/\tilde{a}_{\infty}},k=\frac{\tilde{k}}{\tilde{a}_{\infty}^{2}},\mu_{t}=\frac{\tilde{\mu}_{t}}{\tilde{\mu}_{\infty}} \tag{3-10}$$

Turbulence model

The turbulence model is the basis for developing the transition model, among which the Shear Stress Transport (SST) (Menter, 1994) turbulence model proposed by Menter is one of the most widely used and successful turbulence models. The SST turbulence model combines Wilcox's k-ω turbulence model (Wilcox, 1988) with the k-ε turbulence model by mixing function F_1 so that the SST turbulence model possesses both the strong robustness of the k-ω model in the boundary layer and the independence of the k-ε model in the free flow. The SST mode expression of the two equations is:

$$\frac{\partial(\rho k)}{\partial t}+\frac{\partial(\rho u_{j}k)}{\partial x_{j}}=P_{1}-\beta^{*}\rho\omega k+\frac{\partial}{\partial x_{j}}\left[(\mu+\sigma_{k}\mu_{t})\frac{\partial k}{\partial x_{j}}\right] \tag{3-11}$$

$$\frac{\partial(\rho\omega)}{\partial t}+\frac{\partial(\rho u_j\omega)}{\partial x_j}=\frac{\gamma}{\nu_t}P_1-\beta\rho\omega^2+\frac{\partial}{\partial x_j}\left[(\mu+\sigma_\omega\mu_t)\frac{\partial\omega}{\partial x_j}\right]+2(1-F_1)\frac{\rho\sigma_{\omega 2}}{\omega}\frac{\partial k}{\partial x_j}\frac{\partial\omega}{\partial x_j} \quad (3\text{-}12)$$

The generated item P_1 is calculated as follows:

$$P_1=\tau_{ij}\frac{\partial u_i}{\partial x_j} \quad (3\text{-}13)$$

$$\tau_{ij}=\mu_t(2S_{ij}-\frac{2}{3}\frac{\partial u_k}{\partial x_k}\delta_{ij})-\frac{2}{3}\rho k\delta_{ij} \quad (3\text{-}14)$$

$$S_{ij}=\frac{1}{2}(\frac{\partial u_i}{\partial x_j}+\frac{\partial u_j}{\partial x_i}) \quad (3\text{-}15)$$

Where μ_t is the viscosity coefficient of the turbulent vortex, and its expression is:

$$\mu_t=\frac{\rho a_1 k}{\max(a_1\omega,\Omega F_2)} \quad (3\text{-}16)$$

Table 1 summarizes the closed parameters in the turbulence mode and their standard default values. In addition, γ_1 and γ_2 are also mode constants, which are calculated from other mode constants:

$$\gamma_1=\frac{\beta_1}{\beta^*}-\sigma_{\omega 1}\frac{\kappa^2}{\sqrt{\beta^*}} \quad (3\text{-}17)$$

$$\gamma_2=\frac{\beta_2}{\beta^*}-\sigma_{\omega 2}\frac{\kappa^2}{\sqrt{\beta^*}} \quad (3\text{-}18)$$

The following formula can calculate mode closure coefficients β, γ, σω, σk:

$$\phi=F_1\phi_1+(1-F_1)\phi_2,\qquad(\phi=\beta,\sigma_k,\sigma_w,\gamma) \quad (3\text{-}19)$$

Where φ_1 represents the closed parameters derived from k-ω turbulence mode, and φ_2 represents the closed parameters derived from k-ε turbulence mode.

The mixing function F_1 used to couple k-ω and k-ε turbulence modes is 1 in the boundary layer, and the free incoming flow is 0. Its expression is:

$$
\begin{gathered}
F_1 = \tanh(\Gamma^4) \\
\Gamma = \min[\max(\Gamma_1, \Gamma_3), \Gamma_2] \\
\Gamma_1 = \frac{500\nu}{d^2\omega}, \Gamma_2 = \frac{4\rho\sigma_{\omega 2}k}{d^2(\mathrm{CD}_{k-\omega})}, \Gamma_3 = \frac{\sqrt{k}}{\beta^*\omega d} \\
CD_{k-\omega} = \max\left(2\rho\sigma_{\omega 2}\frac{1}{\omega}\frac{\partial k}{\partial x_i}\frac{\partial \omega}{\partial x_i}, 10^{-20}\right) \\
F_2 = \tanh\left(\Pi^2\right), \Pi = \max\left(2\Gamma_3, \Gamma_1\right) \\
\Omega = \sqrt{2W_{ij}W_{ij}}, W_{ij} = \frac{1}{2}\left(\frac{\partial u_i}{\partial x_j} - \frac{\partial u_j}{\partial x_i}\right)
\end{gathered}
\tag{3-20}
$$

Where d is the shortest distance between the point in the flow field and the wall surface, and Ω is the vorticity tensor.

Transition model

In this paper, a transition model based on Reynolds Averaged Navier-Stokes (abbreviated as RANS) equation was used to simulate dynamic transition. The transition model is $k-\omega-\gamma$ used to simulate the transition (Zhou et al., 2016).

The transition model is based on the concept of non-turbulent pulsation energy and the introduction of intermittent factor transport equation to model convection transition. The most important feature of the transition model $k-\omega-\gamma$ is that it considers the influence of the evolution of unstable disturbance waves in the laminar boundary layer on flow development. The specific modeling method compares the non-turbulent pulsation with turbulent pulsation and models their influence on flow into a uniform form with the vortex viscosity coefficient. Finally, the intermittent factor is the weighting coefficient to obtain the equivalent vortex viscosity coefficient. Subscript "$_{nt}$" marks the contribution of non-turbulent pulsation to the equivalent vortex

viscosity coefficient and the vortex viscosity coefficient of unstable, disturbed waves in the region before the transition is denoted. The specific solution form is as follows:

$$\mu_{nt} = C_{\mu} \cdot \rho \cdot k \cdot \tau_{nt} \tag{3-21}$$

Where C_{μ} is the model constant, k is the total pulsating kinetic energy, and τ_{nt} is the time scale of non-turbulent pulsation. The transition model $k-\omega-\gamma$ models the time scale of the disturbance wave of the first, the second, and the transverse flow models, respectively. The first, second, and transverse flow models are represented by corner symbols "$_{nt1}$", "$_{nt2,}$" an" "cross," respectively. According to whether there is a relative supersonic region in the boundary layer, the time scale can be expressed as:

$$\tau_{nt} = \begin{cases} \tau_{nt1} + \tau_{nt,cross} & ,|M_{rel}| \le 1 \\ \tau_{nt2} + \tau_{nt2} + \tau_{nt,cross} & ,|M_{rel}| > 1 \end{cases} \tag{3-22}$$

The specific form of the time scale of each disturbance model is:

$$\tau_{nt1} = C_2 \cdot \zeta_{eff}^{1.5} / \sqrt{|U|\nu} \tag{3-23}$$

$$\tau_{nt2} = C_3 \cdot \zeta_{eff} / U(y_s) \tag{3-24}$$

$$\tau_{nt,cross} = C_7 \cdot (4\zeta / U_e) \times \left\{ -\exp\left[-C_8 \left(\zeta U_e / \nu_e - 44 \right)^2 \right] \right\} \times \left(W / U_e \right)^{C_9} \tag{3-25}$$

$$\zeta_{eff} = \min(\zeta, C_1 l_T) = \min\left(\frac{d^2 \Omega}{|U|}, \frac{C_1 \sqrt{k}}{\omega} \right) \tag{3-26}$$

Where ζ_{eff} equivalent length scale d represents the minimum distance from the wall and Ω is the modulus of vorticity.

The equivalent vortex viscosity coefficient takes the intermittent factor γ as the weighting coefficient and coupling the vortex viscosity coefficient μ_t obtained from the turbulence model

with the vortex viscosity coefficient corresponding to non-turbulence pulsation μ_{nt} obtained from the transition model. Finally, the following is obtained:

$$\mu_{eff} = (1-\gamma)\mu_{nt} + \gamma\mu_t \tag{3-27}$$

The intermittent factor transport equation in the transition model $k-\omega-\gamma$ can be expressed as:

$$\frac{\partial(\rho\gamma)}{\partial t} + \frac{\partial(\rho u_j \gamma)}{\partial x_j} = \frac{\partial}{\partial x_j}\left[(\mu+\mu_{eff})\frac{\partial\gamma}{\partial x_j}\right]\left(\frac{Ma_\infty}{\mathrm{Re}_\infty}\right) + (P_\gamma - \varepsilon_\gamma)\left(\frac{\mathrm{Re}_\infty}{Ma_\infty}\right) \tag{3-28}$$

Where P_γ and ε_γ are the equation's generated and dissipative terms, respectively.

$$P_\gamma = C_4 \cdot \rho\sqrt{-\ln(1-\gamma)}\left(1 + C_5\sqrt{\frac{k}{u_i u_i}}\right)\frac{d}{\nu}\left|\nabla(u_i u_i)\right| \cdot F_{onset}\ ,\ \varepsilon_\gamma = \gamma P_\gamma \tag{3-29}$$

The function F_{onset} controls the starting position of the transition

$$F_{onset} = 1 - \exp\left(-C_6\frac{\zeta_{eff}\sqrt{k}\,|\nabla k|}{\nu\left|\nabla(u_i u_i)\right|}\right) \tag{3-30}$$

By coupling with the SST turbulence model, the transition model can simulate the process of flow development from laminar to turbulence. The overall framework can be expressed as:

$$\frac{\partial(\rho\gamma)}{\partial t} + \frac{\partial(\rho u_j \gamma)}{\partial x_j} = \frac{\partial}{\partial x_j}\left[(\mu+\mu_{eff})\frac{\partial\gamma}{\partial x_j}\right]\left(\frac{Ma_\infty}{\mathrm{Re}_\infty}\right) + (P_\gamma - \varepsilon_\gamma)\left(\frac{\mathrm{Re}_\infty}{Ma_\infty}\right) \tag{3-31}$$

$$\frac{\partial(\rho k)}{\partial t} + \frac{\partial(\rho u_j k)}{\partial x_j} = \frac{\partial}{\partial x_j}\left[(\mu+\mu_{eff})\frac{\partial k}{\partial x_j}\right]\left(\frac{Ma_\infty}{\mathrm{Re}_\infty}\right) + P_k\left(\frac{Ma_\infty}{\mathrm{Re}_\infty}\right) - \varepsilon\left(\frac{\mathrm{Re}_\infty}{Ma_\infty}\right) \tag{3-32}$$

$$\frac{\partial(\rho\omega)}{\partial t} + \frac{\partial(\rho u_j \omega)}{\partial x_j} = \frac{\partial}{\partial x_j}\left[(\mu+\sigma_\omega\mu_{eff})\frac{\partial\omega}{\partial x_j}\right]\left(\frac{Ma_\infty}{\mathrm{Re}_\infty}\right) + P_\omega\left(\frac{Ma_\infty}{\mathrm{Re}_\infty}\right) - D_\omega\left(\frac{\mathrm{Re}_\infty}{Ma_\infty}\right) + CD_{k\omega}\left(\frac{Ma_\infty}{\mathrm{Re}_\infty}\right) \tag{3-33}$$

When the flow develops into complete turbulence, γ =1, the model is restored to the SST turbulence model.

Boundary condition setting

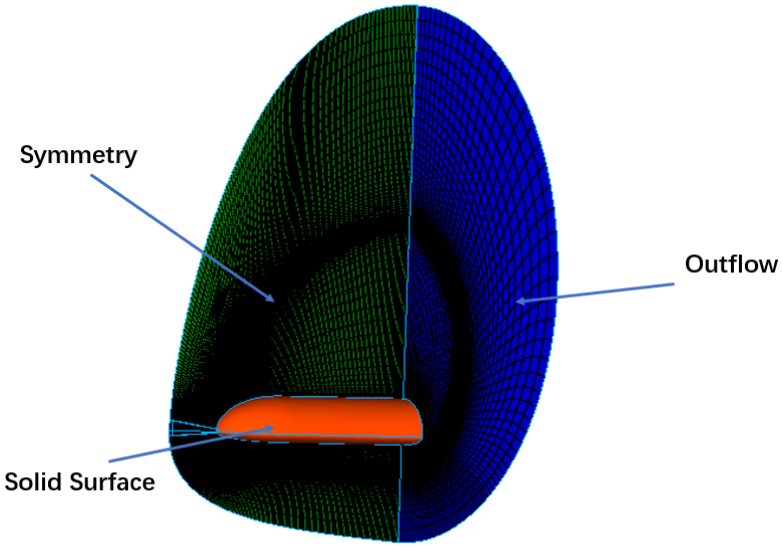

Figure 9 Computing grid diagram

The flow issue is entered into CFD software using an operator-friendly interface, and then the flow problem is transformed from its original form into a form that is acceptable for use by the solver. This is what is meant by "pre-processing." A high-quality computational grid is a key step to doing CFD well, using pointwise software for grid partitioning. The pre-processing module is mainly used for the establishment of CFD geometric models, mesh division, and the addition of physical attributes and boundary conditions.

The grid used in this calculation is output by Pointwise software. Since there is no sideslip angle, a 1/2 grid is used in this calculation, and the amount of grid used for all configurations is about 2 million. The computing grid diagram is shown in **Error! Reference source not found.**.

Isothermal wall 300 K, symmetric boundary, far-field boundary, and exit boundary are used in the rear.

Post-processing

Post-processing, akin to its antecedent phase of pre-processing, has undergone significant research and development in recent years. This phase involves the examination and visual representation of the acquired data. Analysts can scrutinize the data during this stage, drawing conclusions based on the collected results. The data can be depicted in various formats, such as static or dynamic visuals, graphs, or tables.

Upon computing the flow field, a discrete solution for the flow variables becomes available at each mesh element within the domain. Standard interpolation techniques can then be employed to derive the flow variable values at any point within the flow domain. CFD software typically offers robust graphical capabilities for visual analysis of the solution and reporting of various flow quantities. Should the results prove unsatisfactory, the mesh can be refined, or adjustments can be made to the numerical or physical models.

The challenge of determining an aircraft's drag involves calculating the flow regime and velocity. Considering air's compressibility, it is crucial to determine its density at the aircraft's surface. Integrating these factors allows for the evaluation of drag conditions and, consequently, the overall aerodynamic forces exerted on the aircraft. A series of CFD simulations is essential to ascertain the fluid flow rate, impacting the aircraft's drag and lift, and to evaluate the internal mechanical forces ensuring structural integrity. Selecting the appropriate solver tools is imperative to balance simulation accuracy and computational effort, with mesh generation playing a key role in this equilibrium.

Tecplot software emerges as a vital asset in the analysis and post-processing of CFD-generated simulations, with its advanced mathematical algorithms and user-friendly interface facilitating the systematic processing of large and complex data sets. This capability enables engineers to efficiently explore and validate new design concepts. Tecplot offers diverse post-processing functionalities, including contour, surface, and vector plots, allowing for comprehensive visualization of flow patterns, streamlining of flowfield data, and examination of pivotal CFD parameters. Its ability to export data in various formats and animate the progression of CFD simulations provides insights into fluid dynamics behavior under different conditions, enhancing its utility across sectors like aerospace engineering and biomedical research. In this study, Tecplot software was employed to visualize and analyze the data for the four configurations, with the generation of flow field diagrams and graphs to correlate with wind tunnel experimental data.

Findings

In this paperh_{FR} is a heat transfer coefficient obtained based on the Fay-Riddell theory. We use $h_{FR}$to measure the degree of convective heat transfer. Also, in the experiment, boundary layer fluid is represented therefore when h_{FR} changes dramatically, the transition can be judged to occur, thus determining the location of the transition. Using Tecplot software for post-processing, we analyzed the flowfield distribution, and aerodynamic heating curves, including the transition of the four shapes at 30° and 40° AoA, respectively, and extracted the midline data for comparison.

Flowfield analysis

The working condition of the calculation is shown in **Error! Reference source not found.**

Table 4 Working condition of calculation

α, deg	$Re_\infty, 1/m$	M_∞	P_∞, Pa	T_∞, K	ρ_∞, kg/m^3	U_∞,m/s	$h_{FR}, kg/m^2/s$
40	2.73 $\times 10^7$	6.0 3	2091	58.6	1.249 $\times 10^{-2}$	918.2	4.172×10^{-1}

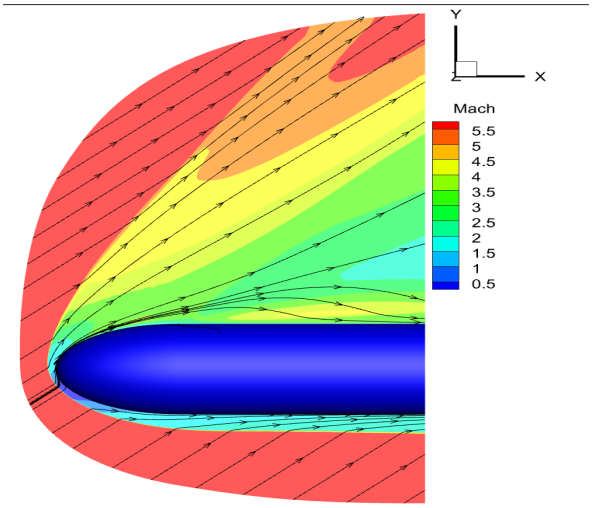

Figure 10 Ellipsled 2.00-1.00 Flowfield

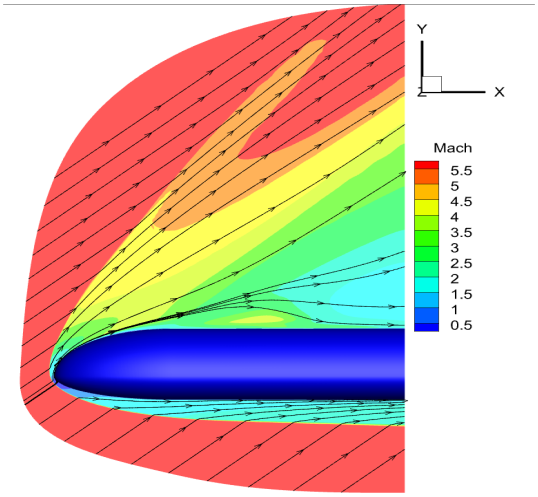

Figure 11 Ellipsled 2.00-0.50 Flowfield

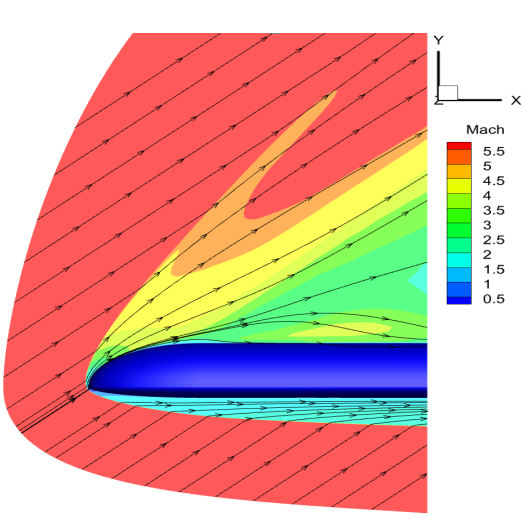

Figure 12 Ellipsled 2.00-0.25 Flowfield

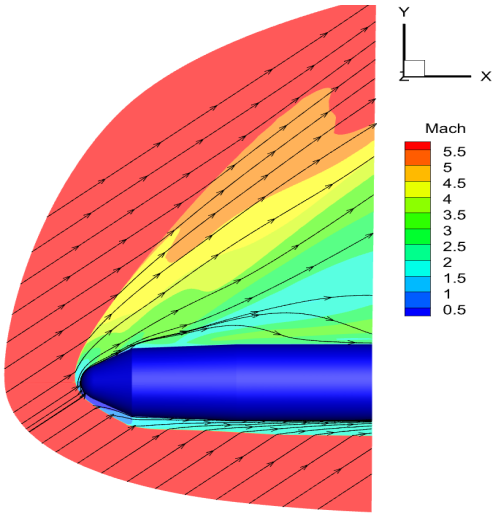

Figure 13 Hammerhead-Nominal Flowfield

Figures 10-13 illustrate the flowfields of 4 different kinds of configurations under the working condition in Table 4.

Aerodynamic heat

Aerodynamic heating is the thermal energy generated from air friction during an aircraft's high-speed flight. This thermal energy significantly impacts the vehicle, causing structural deformation, thermal expansion, and loss of heat transfer, which, in turn, affect the aircraft's performance and safety. The simulations conducted at a Mach number of 6 encompass a Reynolds number range that facilitates the examination of laminar flow, transitional flow, and turbulence. Consequently, this paper focuses on analyzing the aerodynamic thermal phenomena exhibited by various shapes at different angles of attack within both laminar and turbulent flow regimes.

In essence, the implications of aerodynamic heating on vehicles are comprehensive, influenced by a spectrum of factors within the aircraft's internal and external environments. To assure the performance and safety of the aircraft, intricate and meticulous technical approaches must be

employed in the design and manufacturing processes.

The computational conditions for each Ellipsled geometry variant are detailed in Table 5, outlining the specific parameters used for the analysis within the study.

Table 5 working condition of calculation

α, deg	$Re_\infty, 1/m$	M_∞	P_∞, Pa	T_∞, K	ρ_∞, kg/m^3	U_∞,m/s	$h_{FR}, kg/m^2/s$
30	2.49 $\times 10^7$	6.0 2	1879	58.1	1.132 $\times 10^{-2}$	913.8	3.921×10^{-1}
40	2.49 $\times 10^7$	6.0 2	1879	58.1	1.132 $\times 10^{-2}$	913.8	3.921×10^{-1}

Ellipsled 2.00-1.00

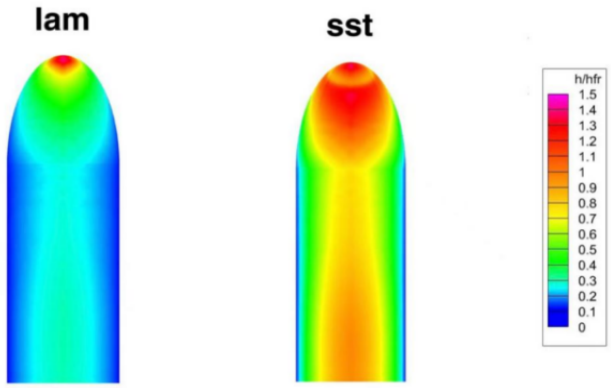

Figure 14 Aerodynamic heat distribution at 30° AoA under laminar and turbulent conditions

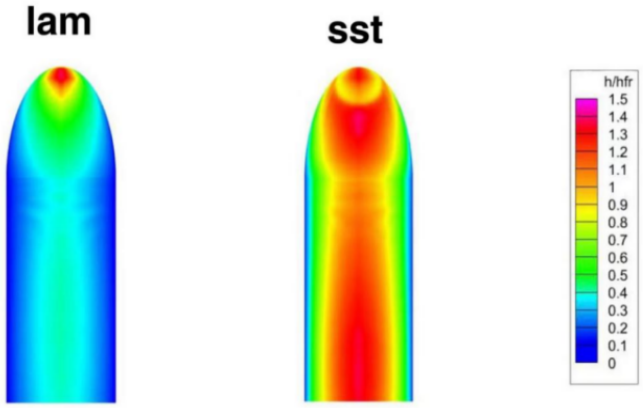

Figure 15 Aerodynamic heat distribution at 40° AoA under laminar and turbulent conditions

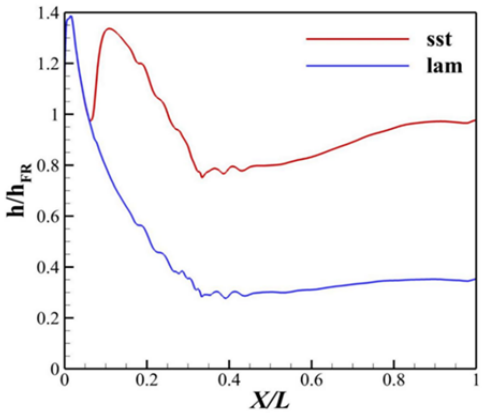

a) the angle of 30°

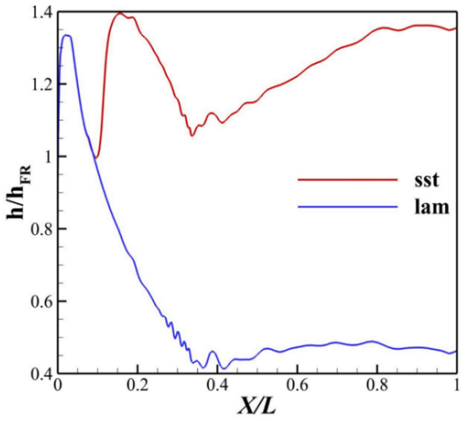

b) the angle of 40°

Figure 16 Comparison of aerodynamic heating curves of Ellipsled 2.00-1.00 under laminar and turbulent conditions

Ellipsled 2.00-0.50

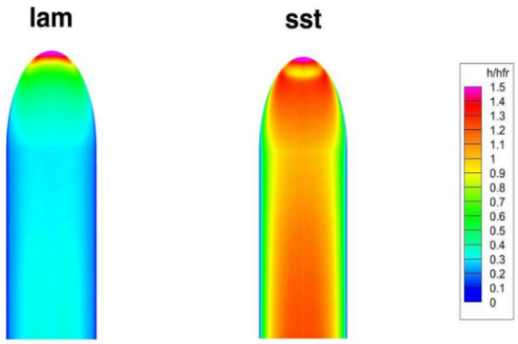

Figure 17 Aerodynamic heat distribution at 30° AoA under laminar and turbulent conditions

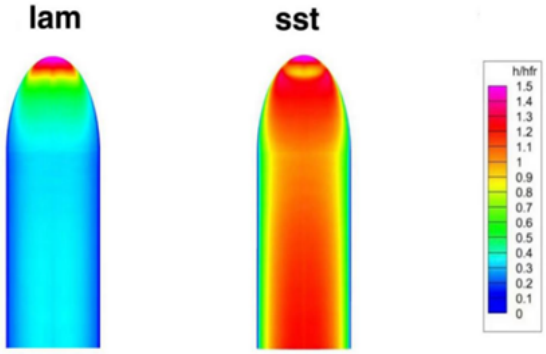

Figure 18 Aerodynamic heat distribution at 40° AoA under laminar and turbulent conditions

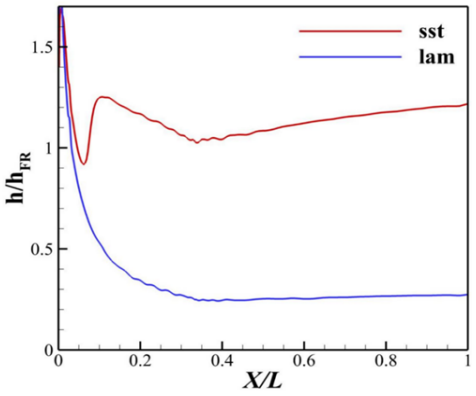

a) the angle of 30°

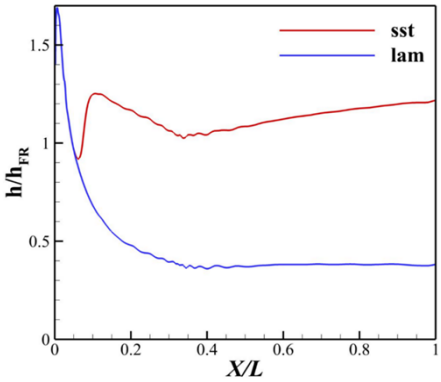

b) the angle of 40°

Figure 19 Comparison of aerodynamic heating curves of Ellipsled 2.00-0.50 under laminar and turbulent conditions

Ellipsled 2.00-0.25

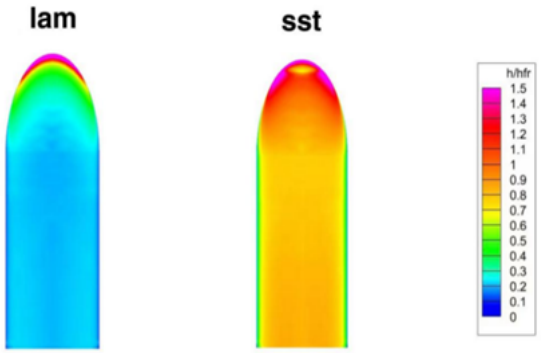

Figure 20 Aerodynamic heat distribution at 30° AoA under laminar and turbulent conditions

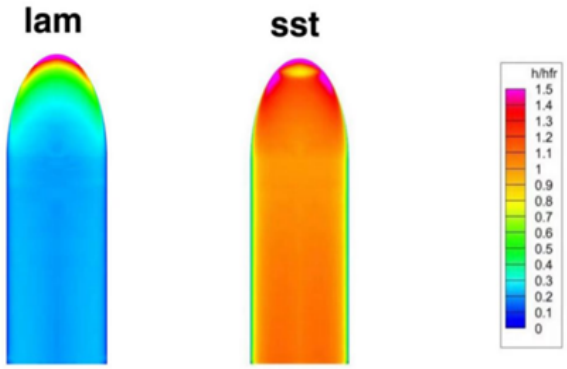

Figure 21 Aerodynamic heat distribution at 40° AoA under laminar and turbulent conditions

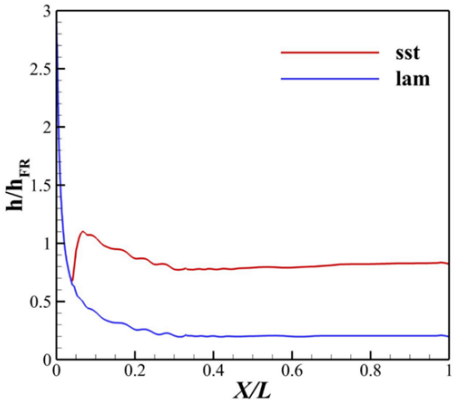

a) the angle of the 30°

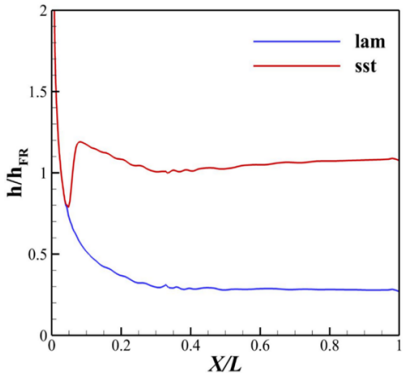

b) angle of 40°

Figure 22 Comparison of aerodynamic heating curves of Ellipsled 2.00-0.25 under laminar and turbulent conditions

Hammerhead-Nominal Configuration

The working condition of calculation for Hammerhead geometry is shown in Table 6.

Table 6 Working condition of calculation

α, deg	$Re_\infty, 1/m$	M_∞	P_∞, Pa	T_∞, K	ρ_∞, kg/m^3	U_∞,m/s	$h_{FR}, kg/m^2/s$
40	2.49 $\times 10^7$	6.0 2	1879	58.1	1.132 $\times 10^{-2}$	913.8	3.921×10^{-1}

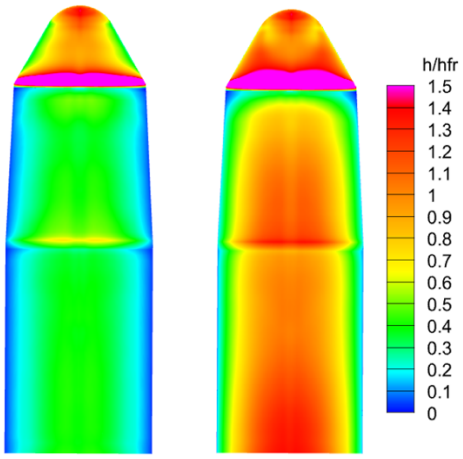

Figure 23 Aerodynamic heat distribution at 40° AoA under laminar and turbulent conditions

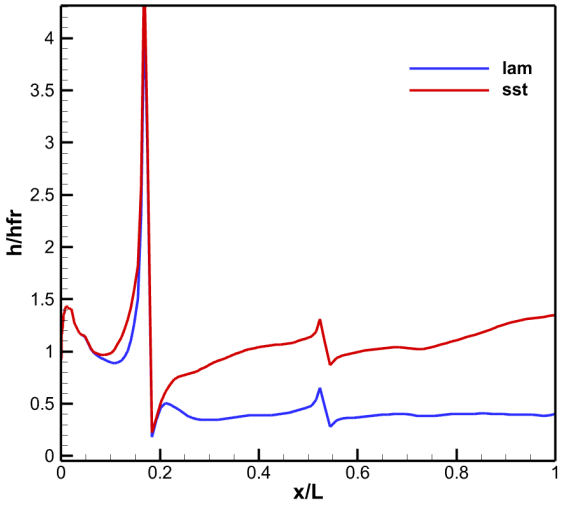

Figure 24 Comparison of aerodynamic heating curves of Hammerhead-Nominal Configuration under laminar and turbulent conditions

Transition

Transition refers to the process of boundary layer fluid changing from laminar flow to turbulent flow under external disturbance. The wall friction and heat flow of the boundary layer in

a turbulent state can reach more than four times that in a laminar state. Therefore, accurate prediction and effective control of transition have a decisive influence on flight drag reduction and thermal protection structure design.

In this chapter, the transition of three shapes of configuration is calculated, Ellipsled 2.00-0.50, Ellipsled 2.00-0.25, and Hammerhead-Nominal. The transition location and heat flow are predicted in each configuration. However, under each working condition, there is no obvious transition phenomenon of Ellipsled 2.00-1.00 in the wind tunnel experiment. Therefore the transition situation has not been studied.

Ellipsled 2.00-0.50

The working condition of the calculation is shown in Table 7.

Table 7 Working condition of calculation

α, deg	$Re_\infty, 1/m$	M_∞	P_∞, Pa	T_∞, K	ρ_∞, kg/m^3	U_∞,m/s	$h_{FR}, kg/m^2/s$
40	2.73×10^7	6.03	2091	58.6	1.249×10^{-2}	918.2	4.172×10^{-1}

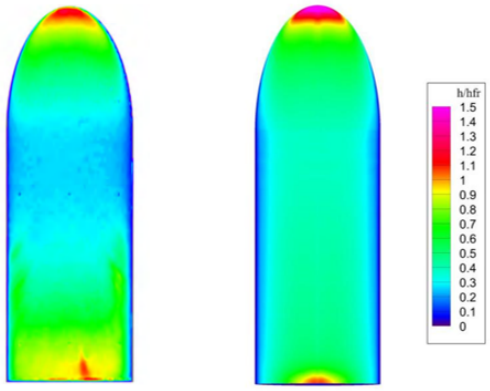

Experiment **CFD**

Figure 25 Ellipsled 2.00-0.5 hFR comparison of experimental values and CFD calculation results

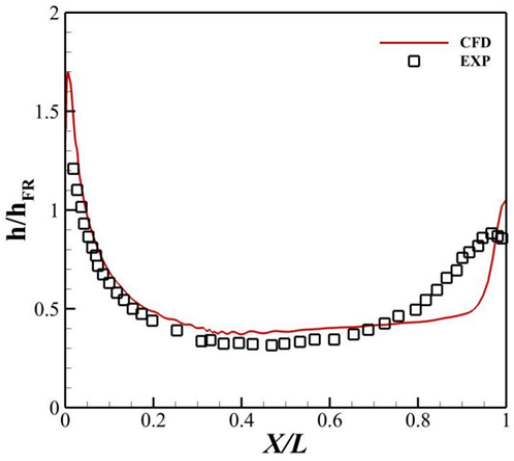

Figure 26 Ellipsled 2.00-0.5 hFR comparison curve of experimental values and CFD calculation results

Ellipsled 2.00-0.25

The working condition of the calculation is shown in Table 8.

Table 8 Working condition of calculation

α, deg	$Re_\infty, 1/m$	M_∞	P_∞, Pa	T_∞, K	ρ_∞, kg/m^3	U_∞,m/s	$h_{FR}, kg/m^2/s$
40	2.24 × 10^7	6.0 2	1667	57.4	1.016 × 10^{-2}	908.0	3.685×10^{-1}
40	2.49 × 10^7	6.0 2	1879	58.1	1.132 × 10^{-2}	913.8	3.921×10^{-1}

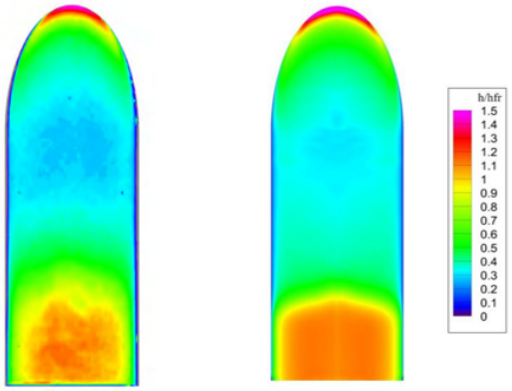

Experiment **CFD**

Figure 27 Ellipsled 2.00-0.25 hFR comparison of experimental values and CFD calculation results, Re=2.24×107 /m

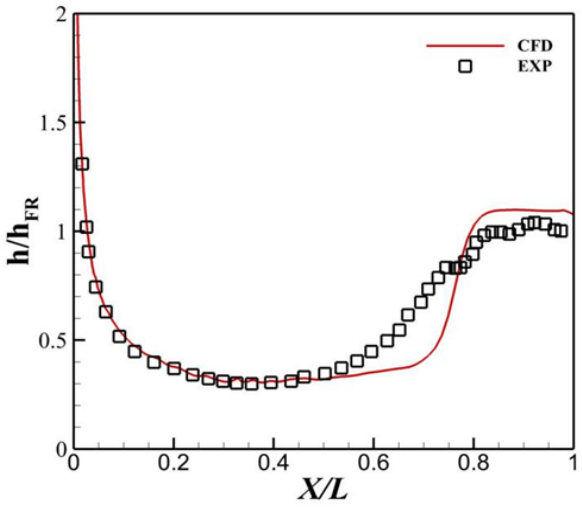

Figure 28 Ellipsled 2.00-0.25 hFR comparison curve of experimental values and CFD calculation results, Re=2.24×10^7/m

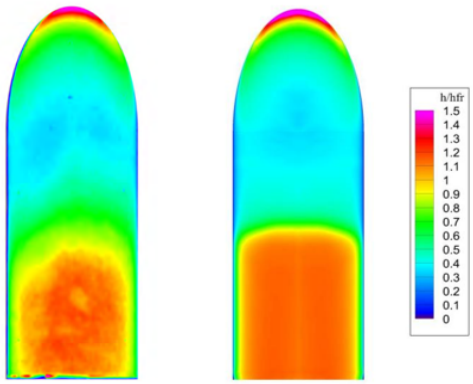

Experiment **CFD**

Figure 29 Ellipsled 2.00-0.25 hFR comparison of experimental values and CFD calculation results, Re=2.49×10^7/m

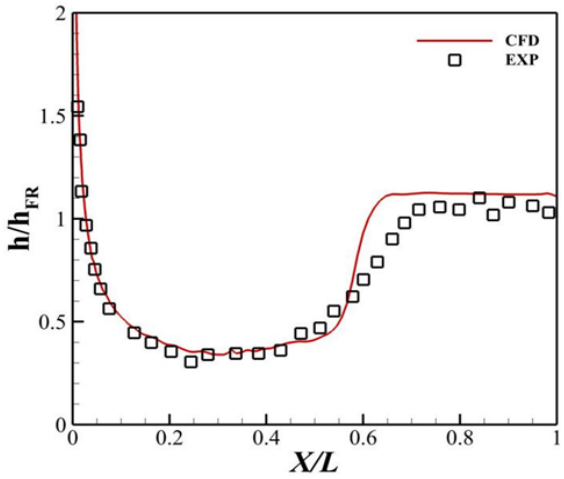

Figure 30 Ellipsled 2.00-0.25 h_{FR} comparison curve of experimental values and CFD calculation results, Re=2.49×10^7/m

Hammerhead-nominal

The working condition of the calculation is shown in Table 9

Table 9 Working condition of calculation

α, deg	$Re_\infty, 1/m$	M_∞	P_∞, Pa	T_∞, K	ρ_∞, kg/m^3	U_∞,m/s	$h_{FR}, kg/m^2/s$
40	2.49×10^7	6.0 2	1879	58.1	1.132×10^{-2}	913.8	3.921×10^{-1}

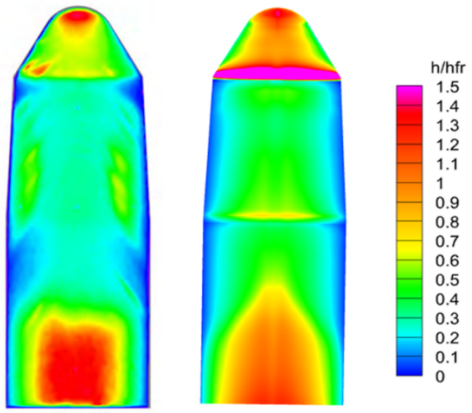

Experiment **CFD**

Figure 31 Hammerhead-Nominal h_{FR} comparison of experimental values and CFD calculation results

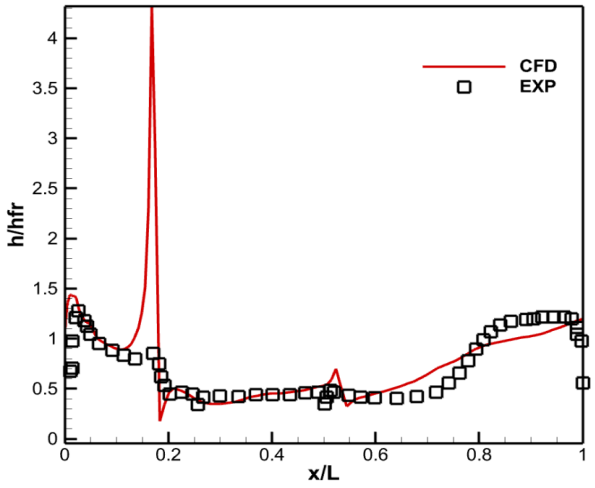

Figure 32 Hammerhead-Nominal h_{FR} comparison curve of experimental values and CFD calculation results

Discussion

To elucidate the flowfield dynamics within each configuration, a profound comprehension of flowfield behavior at hypersonic velocities is imperative. The study of hypersonic flow necessitates an exploration into the high-temperature and high-pressure regimes characteristic of such speeds, coupled with the intricate interactions between bow shockwaves and the contours of aerodynamic surfaces. An exhaustive understanding of the fundamental physics governing hypersonic flows is essential to facilitate an accurate evaluation. This necessitates an engagement with the governing equations of fluid dynamics and the thermodynamic attributes of the gases involved.

Furthermore, a detailed understanding of bow shockwave dynamics and interactions is crucial for determining the influence of aerodynamic surfaces on the flowfield. The bow

shockwave, a critical aerodynamic event prevalent in supersonic aircraft, rocket propulsion, and other aerospace domains, arises when a fluid at high velocity traverses the surface of a curved object. This phenomenon exhibits several distinct characteristics:

1. The fluid temperature remains constant across the bow shockwave, which originates from a differential pressure in the flowfield induced as the fluid circumnavigates a curved surface. This scenario leads to fluid acceleration, compression upon encountering the shockwave, followed by subsequent acceleration. The process predominantly facilitates energy transformation through pressure alterations.

2. The bow shockwave functions as a compression shockwave, with its anterior edge constituting the compression zone and its posterior edge forming the expansion zone. Consequently, both the pressure and density of the gas escalate at the forefront of the bow shockwave and diminish at its rear. This alteration in fluid dynamics can induce variations in fluid velocity, thereby impacting the aerodynamic performance and stability of aircraft.

According to the results in **Error! Reference source not found.-Error! Reference source not found.**, under the working condition Re=2.73×10^7/m, Mach=6.03, due to the high incoming Mach number, a strong bow shock wave is formed under the windward side of the body, and the flow slows down. As can be seen in each figure, the flow direction is compressed on the leeward side, and most of the body surface is attached flow.

The heating distributions for the ellipsled configurations are depicted in Figures 14-22. The boundary-layer transition was detected at the model centerline for each of the three ellipsled configurations, with the exception of the Ellipsled 2.00-1.00 configuration, which had the sharpest-nosed axisymmetric profile. On the axisymmetric Ellipsled 2.00-1.00 configurations, "feathered" heating patterns of increasing strength with Reynolds number were created outboard

of the configuration oriented away from the centerline.

The strength of the patterns increased as the Reynolds number increased. These patterns are probably illustrative of vortices resulting from the transition of cross-flow. On the configurations of the ellipsled, these kinds of patterns were not seen at all. On the Ellipsled 2.00-0.25 configuration, the greatest amount of fully developed turbulent flow and the highest levels of turbulent heating were created. An overexpansion and recompression shock were created on the Ellipsled 2.00-0.25 configuration, as illustrated in Figure 24, and directly downstream of the nose–cylinder junction, according to the analysis of computed heating distributions. In a turbulent flow, almost every region of the shape receives a high amount of heat, which could cause an explosion and a failure in the design.

The heat distributions for the hammerhead geometry are depicted in Figures 23-24. The Hammerhead configurations produced flow patterns that were more intricate than those created by the ellipsled arrangement. This significant disparity can be explained, at least in part, by the discontinuities in the geometric slopes that exist between the various segments. The proximity of the stagnation point to the intersection of the nose and the first cone section is another factor that may help to explain the disparity. In Figure 23, it can be observed that in laminar flow, the heating existed at the nose of the configuration, while for turbulent flow, it is observed to experience high temperatures causing heavily turbulent flow. However, in Figure 24, it is proven that the turbulent flow is always higher than the laminar flow in any position of x/l.

Given the turbulent environment at 40^{o} AoA with Ellipsled geometry, comparing the h/h_{FR} given X/L = 1, the value of h/h_{FR} is higher for Ellipsled 2.00-1.00 than for Ellipsled 2.00-0.50. Similarly, the CFD results revealed that h/h_{FR} is lower at the same point with Ellipsled 2.00-0.25 than with both Ellipsled 2.00-0.50 and Ellipsled 2.00-1.00.

For both Ellipsled and Hammerhead geometries, the h/h_{FR} for laminar are consistently lower than those of the turbulent irrespective of the angle of attack. On the other hand, comparing the worst scenario of the Ellipsled with Hammerhead geometries, our CFD output indicated that Ellipsled geometry emerged as a better option both at X/L = 1, as well as at the highest peak of h/h_{FR} in general.

Transition

Obvious transition can be observed in the shape of flow Ellipsled 2.00-0.25 and Hammerhead-Nominal, and the Ellipsled 2.00-0.50 shape transition phenomenon is relatively weak. By comparing the results of the CFD calculation with the experimental values in the wind tunnel, the model can predict the transition under different shapes and different working conditions. The transition position of individual working conditions is predicted relatively late, and the heat flow in the whole turbulent zone is high.

The transition conditions in each configuration were predicted, as shown in **Error! Reference source not found.-Error! Reference source not found.**. For Ellipsled 2.00-0.50, it can be observed that the transition is really low in the experimental result and CFD results. This is because the heat experienced by the body's surface is relatively low, making it difficult to experience turbulent flow. However, when the body faces a high heat during ascending, the result would be vice-versa. In Ellipsled 2.00-0.25, different Reynolds number were applied in the simulation. At $Re=2.24\times10^7$/m, the transition to turbulent flow can be seen clearly in Figure 27. Comparing **Error! Reference source not found.** with **Error! Reference source not found.**, it is visible that the result with $Re=2.49\times10^7$/m experiences a highest transition among the rest of the ellipsled configurations and also a hammerhead-nominal configuration.

The boundary-layer transition for the Hammerhead geometry, shown in **Error! Reference**

source not found.-Error! Reference source not found., did not occur in the hammerhead nominal configuration until about halfway down the last cylindrical segment. In addition, feathering patterns on the Hammerhead-nominal geometry that was comparable to those on the axisymmetric ellipsled were seen toward the outboard of the second cone section, which was an indication of cross-flow transition.

Comparisons between turbulent predictions and transitional/turbulent data were more complex. Because the turbulence model used does not predict transition onset or the length of the transition region to fully-turbulent flow, these parameters were specified to match the experimental data. However, while the transition onset location could be specified fairly accurately, the transition regime length and distribution were more difficult to match within the limits of this model. Thus, differences greater than the experimental uncertainty were produced both within and downstream of the transition region. However, the comparisons were much better for the cases where a significant length of fully turbulent flow was produced, notably on the Ellipsled-2.00-0.25, configurations at the higher Reynolds numbers. These observations pertain only to the centerline of the geometries, where stream-wise transition onset was dominant. No attempt was made to match the cross-flow transition patterns that were noted on several of the configurations.

Conclusion

Firstly, this paper investigates the research background and relevant literature, focusing on the relevant applications and advantages of the "Mid Lift-to-Drag Ratio Entry Vehicles" (ML-DREVs). It is found that the ML-DREVs has the advantages of large volume, good deceleration effect during reentry, easy flight attitude control and other advantages, and has good aerodynamic characteristics.

Secondly, in this paper, the results of laminar flow, turbulence and transition of four shapes under different working conditions are calculated, and the results are compared with the experimental values of wind tunnel. The results show that the aerodynamic heating effect is more obvious with the increase of the AoA under the same condition with the same shape. For Ellipsled shapes, as an angle of attack decreases, the aerodynamic heating effect of the surface weakens, indicating that the aerodynamic heating effect of all Ellipsled different shapes are also low and reliable in any space missions. Under the same calculation condition with the same shape, with the increase of the angle of attack, the aerodynamic heating effect on the windward side is more obvious and high after the flow passes through the bow shock wave. For Hammerhead-Nominal shape, due to the discontinuous variation of the shape, the calculated results increase significantly at the prominent position, and the turbulent heating effect is stronger than that of laminar flow.

Thirdly, the higher the Reynolds number, the more likely transition is to occur, transition is a very dangerous aerodynamics phenomenon, which will have a serious impact on flight safety. The study of boundary layer transition has urgent engineering needs and is one of the key issues that must be considered in the design of aircraft. Accurate prediction of boundary layer transition location is of great importance to the design of aerodynamic layout, thermal protection and propulsion system of aircraft. The transition model $k-\omega-\gamma$ used in this paper can basically predict the transition situation under different shapes and different working conditions, but there are also some shortcomings, the transition position of some working conditions is different from the experimental value, the heat flow in the whole turbulent zone is also high.

Overall, the aerodynamic design and the performance analysis of Mid Lift-to-Drag Ratio Entry Vehicles was completed using the three major methods of CFD which are pre-processing,

solving and post-processing. After carrying out the experiment, except for Ellipsled-2.00-1.00, all geometries experienced center-line, stream-wise boundary-layer transition. The Ellipsled-2.00-0.25 and Hammerhead-nominal configurations created regions of fully developed turbulent flow, although the other configurations also experienced intensely turbulent flow. On the Ellipsled-2.00-1.00 and Hammerhead-nominal geometries, "feathered" heating patterns indicating cross-flow transition were also seen in addition to stream-wise transition. For first-order mission planning and analysis purposes, fully turbulent predictions based on the $k-\omega-\gamma$ turbulence model can be used to constrain the dataset, but more accurate and realistic forecasts call for more sophisticated computational models.

References

[1] Costa A. Application of Computational Aerodynamics Methods to the Design and Analysis of Transport Aircraft. 1978.

[2] Bertin J J. Hypersonic Aerothermodynamics [M]. 1994.

[3] Jortner J. Comprehensive Composite Materials II || 5.16 Applications of Carbon/Carbon Composites [J]. 2018:421-436.

[4] Space Shuttle Launch Motion Analysis [EB/OL] - NASA, NASA [2023-05-18].

[5] O. Uyanna and H. Najafi, "Thermal Protection Systems for Space Vehicles: A Review on Technology Development, Current Challenges and Future Prospects," *Acta Astronautica*, vol. 176. Elsevier Ltd, pp. 341–356, Nov. 01, 2020. doi: 10.1016/j.actaastro.2020.06.047.

[6] Bradley F, "SpaceX Relies on Stainless-Steel for Starship Mars Rocket" [EB/OL]. [2023-05-17].

[7] Trevino L. SpaceX Dragon Reentry Vehicle: Aerodynamics and Aerothermodynamics with Application to Base Heat-Shield Design [J]. Georgia Institute of Technology, 2008.

[8] Fu M, Gao S, Wang C. Safety-Guaranteed Course Control of Air Cushion Vehicle with Dynamic Safe Space Constraint [J]. Journal of Control Science and Engineering, 2018, 2018:1-7.

[9] Keys A S, Hall J L, Oh D, et al. Overview of a Proposed Flight Validation of Aerocapture System Technology for Planetary Missions[C]// 42nd AIAA/ASME/SAE/ASEE Joint Propulsion Conference & Exhibit. 2006.

[10] Wang Y, Yang S, Zhang D, et al. Design of Waverider Configuration with High Lift-Drag Ratio[J]. Journal of Aircraft, 2007, 44(1):144-148.

[11] Hollis B R, Hollingsworth K E. Laminar, Transitional, and Turbulent Heating on Mid Lift-

to-Drag Ratio Entry Vehicles [J]. Journal of Spacecraft and Rockets, 2013, 50(5):937-949.

[12] Wu, J. C. Theory for Aerodynamic Force and Moment in Viscous Flows [J]. AIAA Journal, 1981, 19(4):432-441.

[13] Daryabeigi K. Thermal Analysis and Design of Multi-Layer Insulation for Reentry Aerodynamic Heating [J]. Journal of Spacecraft and Rockets, 2002, 39(4):509-514.

[14] Office U. Aviation and the Environment. Transition to Quieter Aircraft Occurred as Planned, but Concerns About Noise Persist [J]. Government Accountability Office Reports, 2001.

[15] Tu J, Guan H Y, Liu C. Governing Equations for CFD—Fundamentals [M]. 2008.

[16] Menter F R, Two-Equation Eddy-Viscosity Turbulence Models for Engineering Applications [J]. AIAA Journal, 1994, 32:1598-1605.

[17] Wilcox D C. Reassessment of the Scale-Determining Equation for Advanced Turbulence Model, AIAA Journal, 1988, 26:1299-1310.

[18] Zhou L, Yan C, Hao Z H, et al. Improved k-ω-γ Model for Hypersonic Boundary Layer Transition Prediction [J]. International Journal of Heat and Mass Transfer, 2016, 94:380-389.